Journal of *Marine Science and Engineering*

Article

Influence of Various Stator Parameters on the Open-Water Performance of Pump-Jet Propulsion

Fuzheng Li [1,2], Qiaogao Huang [1,2,*], Guang Pan [1,2], Denghui Qin [1,2] and Han Li [1,2]

1 School of Marine Science and Technology, Northwestern Polytechnical University, Xi'an 710072, China; jinglelfz@mail.nwpu.edu.cn (F.L.); panguang@nwpu.edu.cn (G.P.); qindenghui@mail.nwpu.edu.cn (D.Q.); Lihan_nwpu@mail.nwpu.edu.cn (H.L.)
2 Key Laboratory of Unmanned Underwater Vehicle, Northwestern Polytechnical University, Xi'an 710072, China
* Correspondence: huangqiaogao@nwpu.edu.cn

Abstract: In order to improve the hydrodynamic performance of pump-jet propulsion (PJP) when matching stator with the rotor, the RANS method with SST k-ω turbulence model is employed to study the influence of six kinds of stator parameters, which are classified into three groups, i.e., stator solidity, stator angles and rotor–stator spacing (S). Results show that the stator solidity involves the blade number (Ns) and chord length (L), has an obvious acceleration effect at and after stator, and produces a higher thrust and torque with a slight efficiency change. Further comparing Ns and L results, we find greater distinctions between the two cases when stator solidity is greatly adjusted. Three stator angles, i.e., stagger angle (α), lean angle (γ), and sweep angle (β), are studied. The α has the biggest effect on the thrust, torque, and efficiency; meanwhile, it shifts the advance number that corresponds to maximum efficiency. The effect of γ is similar to α, but its influence is far less than α. However, there is little difference between various β cases except for off-design conditions, where the efficiency drops dramatically as β increases. The S has a slight effect on PJP performance. Even though S decreases 34% relative to the original PJP, the rotor thrust and torque increase by less than 1%. In addition, we compare torque balance locations under various parameters, and each component force is analyzed in detail to explain the reason for performance variation. The present work is conducive to future optimization in PJP design.

Keywords: pump-jet propulsor; SST; stator solidity; stator angle; rotor–stator spacing

Citation: Li, F.; Huang, Q.; Pan, G.; Qin, D.; Li, H. Influence of Various Stator Parameters on the Open-Water Performance of Pump-Jet Propulsion. *J. Mar. Sci. Eng.* **2021**, *9*, 1396. https://doi.org/10.3390/jmse9121396

Academic Editor: Alon Gany

Received: 27 October 2021
Accepted: 24 November 2021
Published: 7 December 2021

1. Introduction

The pump-jet propulsion (PJP), which consists of a stator (a stationary blade row), a rotor (a rotating blade row), and a duct, is a special type of underwater thruster. PJP has been widely used for various underwater vehicles. According to the position of the stator, there are two types of PJP: pre-swirl PJP and post-swirl PJP. The submarines and some offshore vessels generally adopt the former for noise reduction [1]. In contrast, underwater vehicles such as torpedoes typically employ post-swirl PJP, for the post-stator can recover part of the wake energy that is lost with conventional propellers. Hence, the stator generates more thrust and improves the open-water efficiency of PJP.

In earlier years, PJP research mainly focused on the design method. Mccormick et al. [2] are the first academics who discussed the design of a post-stator PJP. They performed the numerical evaluation of the efficiency and cavitation of PJP. The shroud and propeller were replaced by an equivalent system of ring source and sinks, ring vortices, and vortex filaments. Henderson et al. [3] introduced a method for the design of PJP. A quasi-one-dimensional method of blade design was described that used compressor data. Meanwhile, the arrangement of shroud and vanes is discussed. Furuya et al. [4] presented a report describing the blade-to-blade design with corrections due to the three-dimensional approach.

There is some literature about hydrodynamic research on PJP by experimental and numerical methods. In the experimental study, Zierke et al. [5] are earlier researchers who performed various test methods in the underwater turbomachine with stator. They conducted experimental measurements of a high Reynolds number axial pump in the Applied Research Laboratory (ARL) at Penn State. Flow visualization and velocity measurement by laser doppler velocimeter (LDV) were carried out. In addition, both slow-response and fast-response pressure probes were used to test pressure fluctuation. Suryanarayana et al. [6–8] conducted a series of experiments of PJP on an axisymmetric underwater body. The investigation of PJP was tested at a wind tunnel, which focuses on the axial velocity and tangential velocity, the self-propulsion point, thrust magnitude, and torque balance. In addition, experiments at the cavitation tunnel showed that the inception position took place at the rotor tip at a high advance ratio and the leading edge of the suction side at a low advance ratio. However, the duct and stator were free from cavitation. Shirazi et al. [9] also investigated a post-swirl PJP on a full-scale underwater vehicle experimentally and numerically. The experiments include the bollard pull, self-propulsion, and bare hull resistances were conducted to validate the design procedure and verify the numerical results. Further conditions in which PJP works were numerically studied.

In numerical simulation, many academics utilized the RANS method with various turbulence to study PJP; Lee et al. [10] investigated an IGV/rotor propulsion pump using a standard k-ε turbulence model with a low-Reynolds-number approach near the wall. Results such as blade loadings and wake vortex patterns are compared with Zierke's [5] experimental results. The authors of [11–13] also used the k-ε model to investigate the hydrodynamic performance of PJP in torpedo propulsion. Park et al. [14,15] presented a numerical simulation of the waterjet propulsion system and single-stage ducted marine propeller, respectively; both of which solved RANS equations with the k-ε model. Huyer [16] also employed the k-ε model to study the lateral force of a post-swirl propulsor under a controllable pitch stator; both ducted configuration and open case were researched. Ahn [17] studied a pump-jet with and without a ring by solving the Spalart–Allmaras equation. The ring cases showed lower vortex strength at the tip. The tip clearance is a key factor for the shrouded rotor and has been a research hotspot for PJP. The authors of [18–21] numerically investigated the influence of tip clearance on post-stator PJP. Results showed that efficiency is closely related to the size of clearance due to the energy loss generated by tip leakage vortex (TLV). The larger the tip clearance size, the lower efficiency of PJP, while the efficiency remains unchanged when it increases to a certain value. The tip vortices, including tip separation vortex (TSV) caused by separation at the leading edge of the rotor and TLV, are also influenced by clearance. As the tip clearance size increases, the TSV spreads toward the suction side. Decreasing the advance ratio (increasing rotation speed or decreasing the inlet velocity) will reinforce the vortices and make the cavitation phenomenon more possible to happen.

Reviewing the previous literature, most researchers focus on the hydrodynamics of the rotor and flow details around the rotor, especially the tip clearance between the rotor and duct inner surface. Little research has been conducted on pre-swirl stator parameters except for [22], which mainly investigated the rotor fluctuation but ignored some important results of PJP components, such as the stator force, stator torque, and duct force. From Yu's work, it is obvious that the pre-whirl stator has a significant impact on PJP global performance. The fundamental reason is that the hydrofoil performance [23] of rotor blade is influenced by the inflow condition caused by various stator parameters. The comprehensive study of stator parameters is worthwhile for future PJP design. In this paper, six kinds of stator parameters, organized into three groups, are thoroughly studied based on the RANS method. Apart from the hydrodynamics of all components of PJP, we emphasize the flow field between stator and rotor. The layout is as follows:

Section 2 presents the governing equations and the details of numerical discretization method. In Section 3, the geometry of prototype PJP and the definition of stator parameters are given. The computational domain and numerical setup are described in detail. Then, we perform the validation of the numerical method. Section 4 presents the detailed hydrodynamic results of PJP with various parameters. Finally, Section 5 gives the summary of key results.

2. Numerical Simulation Methods

PJP works in a uniform flow, and the fluid is water at a constant temperature, and thus heat transfer effect is neglected. Due to an extremely low Mach number, the water is treated as an incompressible fluid. In the present work, the steady simulation is adopted to investigate the open-water performance of PJP under the different stator parameters. Reynolds Averaged Navier–Stokes (RANS) equations include mass conservation equation and momentum conservation equation are:

$$\frac{\partial U_i}{\partial x_i} = 0 \tag{1}$$

$$\rho \overline{u}_j \frac{\partial \overline{u}_i}{\partial x_j} = \rho \overline{F}_i - \frac{\partial \overline{p}}{\partial x_i} + \frac{\partial}{\partial x_j}\left(\mu \frac{\partial \overline{u}_i}{\partial x_j} - \rho \overline{u_i' u_j'} \right) \tag{2}$$

In the equations, ρ is water density, x_i and x_j are cartesian coordinate components (i = 1, 2, 3; j = 1, 2, 3), and F represents the mass force of an element, such as gravity. For the present work, the F equals to zero. μ and p are the dynamic viscosity and pressure, respectively. u_i and u_j are the absolute velocity component. $\rho\overline{u_i' u_j'}$ is the Reynold stress. $\overline{u}_i$ and $\overline{u}_j$ represent the time-averaged item, the turbulence model is needed for the closure of Equation (2).

The SST k-ω turbulence model is a two-equation eddy-viscosity model proposed by Menter [24], which has become widely used in flow simulation of underwater vehicles and PJP [25–31]. The shear stress transport (SST) formulation combines the best of k-ω model and k-ε model, is able to investigate a model of low Reynolds number without using the wall function method. In the free-stream far away from the wall, the SST can freely switch to the k-ε formulation and thus avoids the common problem exists in k-ω formulation that the model is too sensitive to the inlet free-stream turbulence conditions. Meanwhile, the SST has a better behavior in adverse pressure gradients and separating flow. Qin [19] carried out numerical simulations of PJP with three different turbulence models, namely standard k-ε, realizable k-ε, and SST k-ω turbulence models. The results showed that the SST configuration is much more accurate. Therefore, the SST k-ω formulation is chosen to study the performance and flow characteristics of PJP. The turbulent kinetic energy k and specific dissipation rate ω formulations can be written as follows:

$$U_j \frac{\partial k}{\partial x_j} = P_k - \beta^* k\omega + \frac{\partial}{\partial x_j}\left[(\nu + \sigma_k \nu_T) \frac{\partial k}{\partial x_j} \right] \tag{3}$$

$$U_j \frac{\partial \omega}{\partial x_j} = \alpha {S_0}^2 - \beta\omega^2 + \frac{\partial}{\partial x_j}\left[(\nu + \sigma_\omega \nu_T) \frac{\partial \omega}{\partial x_j} \right] + 2(1 - F_1)\sigma_{\omega 2} \frac{1}{\omega} \frac{\partial k}{\partial x_i} \frac{\partial \omega}{\partial x_i} \tag{4}$$

where the P_k is the production rate of turbulence used to prevent the built-up of stagnation regions:

$$P_k = \min\left(\tau_{ij} \frac{\partial U_i}{\partial x_j},\ 10\beta^* k\omega \right) \text{ with } \tau_{ij} = \nu_T \left(\frac{\partial U_i}{\partial x_j} + \frac{\partial U_j}{\partial x_i} \right)$$

To properly predict the onset and amount of flow separation from the surface, the eddy-viscosity ν_T should be limited, where $v_T = a_1 k / \max(a_1\omega,\ SF_2)$. Notice that $v_T = \mu_T/\rho$. S_0 is an invariant measure of strain rate and F_2 is a blending function similar to F_1. Specific formulations and constant values can be found in reference [32].

In the present work, the Ansys/CFX solver is employed to numerically investigate the global performance of PJP. The solver uses the element-based finite volume method. The governing equations are reorganized in the volume integral and surface integral forms and then discretized with each element. The advection scheme for four equations from (1) to (4) all adopt a high-resolution scheme to ensure a more accurate result and good robustness.

3. Numerical Simulation of PJP

3.1. Model Geometry

Figure 1 shows the typical model-scaled PJP. The pre-swirl stator with eight blades is fixed on the conical hub, which is the extension of the submarine tail and has the same conical degree. The six-post rotor blades are installed on a cylindrical hub, with a tip clearance equal to 1 mm. In this paper, the rotor has a diameter of D_r = 146 mm. The area ratio and hub diameter ratio of the rotor are 0.8 and 0.3, respectively. Both the profile curves of stator hub and shroud are not parallel to the flow direction, thus resulting in unequal diameters of stator at upstream and downstream, which are D_{sin} = 101.8 mm and D_{sout} = 91.6 mm, respectively. The duct length is Ld = 177.8 mm, and the diameters of inlet and outlet are D_{in} = 210.4 mm and D_{out} = 146.0 mm, respectively.

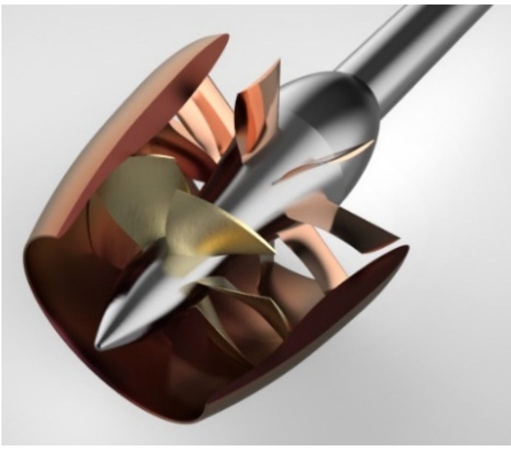

Figure 1. The pump-jet propeller model.

At present, we classify six stator parameters into three groups, i.e., stator solidity, stator angle, and rotor stator spacing (S). The first includes two parameters, the blade numbers (N_s) and chord length (L). The second contains three angles, as shown in Figure 2.

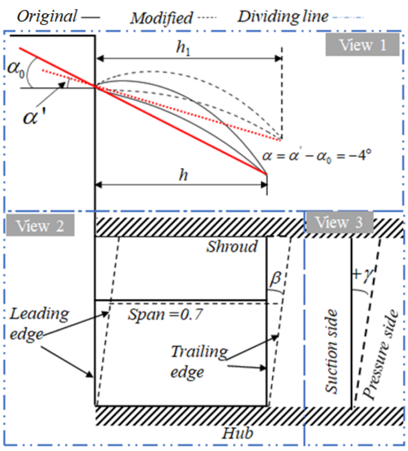

Figure 2. Stator angles in three views.

In Figure 2 view1, i.e., the circumferential view, the original foil and the modified foil at 0.7 span are presented. We adjust the stagger angle (α) of the original model with a step of 4°. However, the blade height (h) increases to h_1 when decreasing α. In order to exclude the influence of blade height on performance of PJP, the chord length (C) is scaled in a proper ratio. The scaled ratio in Figure 2 should be h_1/h.

In Figure 2 view2, i.e., the meridional view, a swept blade with a sweep angle β = 4° in dashed line is shown.

In Figure 2 view3, i.e., the axial view, the solid line, and dashed line are the leading edge of the stator. The lean angle (γ) with a positive value means that the blade leans to the pressure side. Accordingly, negative γ denotes blade leans to the suction side.

The third parameter S is the axial distance between the trailing edge of the stator and the leading edge of the rotor at the root of the blade. It will be modified by translating the stator blade along the axial direction with a step 5 mm and treated as a dimensionless value normalized by D_r. The S for the original PJP is 0.35 D_r.

In the present work, five sets of cases for each parameter will be studied. The computational cases are listed in Table 1.

Table 1. Computational cases for each stator parameters.

Case ID	Stator Parameters					
	Solidity		Angle			Rotor–Stator Spacing
	N_s	L	α	β	γ	S
1	6	6/8C	−8°	−8°	−4°	$0.35D_r$ (origin)
2	7	7/8C	−4°	−4°	0° (origin)	$0.32D_r$
3	8 (origin)	1.0C (origin)	0° (origin)	0° (origin)	4°	$0.29D_r$
4	9	9/8C	4°	4°	8°	$0.26D_r$
5	10	10/8C	8°	8°	12°	$0.23D_r$

3.2. Mesh and Numerical Setup

The entire computational domain is divided into three subdomains: external domain, stator domain, and rotor domain. The external domain is shown in Figure 3. PJP works in a cylindrical tunnel with a length of $15D_r$, and a radius of $5D_r$. The inlet is located $5D_r$ upstream of the rotor, and the outlet is located $10D_r$ downstream of the rotor. Both the stator and rotor domains are generated by a single periodic domain that contains one blade.

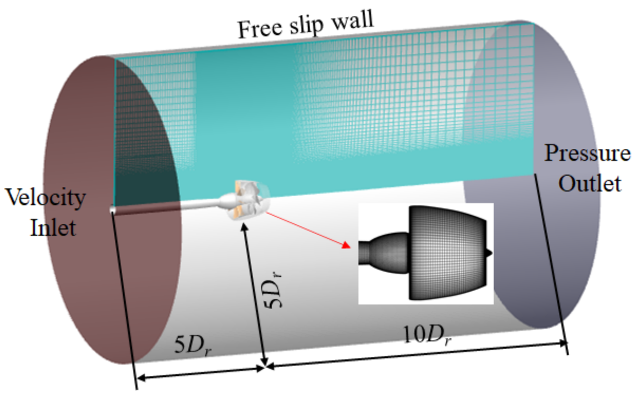

Figure 3. The mesh of external domain and boundary conditions.

Figure 4 shows the coarse grid, the medium grid, and the fine grid of the single domain of rotor and stator. Table 2 lists the number of meshes. The relation between y^+ and the width of the first cell to the wall y is driven by the Blasius equation, expressed as follows:

$$y = 6\left(\frac{V_{ref}}{\nu}\right)^{-\frac{7}{8}}\left(\frac{L_{ref}}{2}\right)^{\frac{1}{8}} y^+ \quad (5)$$

where the V_{ref} is reference velocity, defined as $\sqrt{V_A^2 + (\pi n D_r)^2}$ (V_A denotes the inflow velocity, n denotes the rotation speed). The L_{ref} is reference length, corresponding to the chord length of rotor blade at $r/R = 0.75$. According to Equation (5), the height of first layers, under the typical operating condition of V_A = 2.6 m/s and n = 20 r/s, is 2×10^{-6} m for all solid surface except the tunnel wall.

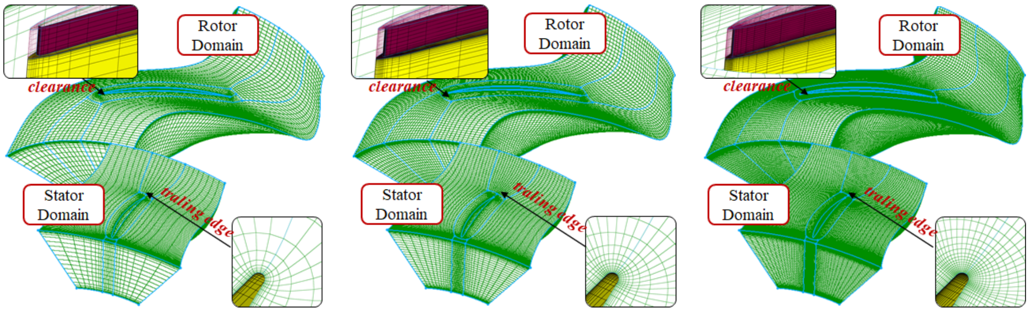

Figure 4. Structure mesh of stator and rotor domain (from **left** to **right**: coarse, medium, fine).

Table 2. Mesh number.

Mesh Groups	ID	Stator Domain (M)	Rotor Domain (M)	External Domain (M)	Total (M)
fine	1	5.13	6.07	3.73	14.92
medium	2	1.35	1.45	2.69	5.49
coarse	3	0.52	0.61	0.87	2.01

The boundary conditions can be seen in Figure 3. A uniform inflow velocity V_A is added at the inlet boundary, and the turbulence intensity is set to 1%. For outlet boundary, an average static pressure of zero is imposed to simulate the far-field. The solid surface of all PJP components is consider to be the no-slip wall. The outer tunnel wall is set to a free-slip wall. In addition, three subdomains need to be connected with the interface boundary. There are three types of interfaces provided by CFX for frame change models, the mixing plane, frozen rotor, and transient rotor–stator methods. Among them, the frozen rotor is the most useful way to produce a steady-state solution for the multi-frame problem, and is adopted in this work. The external domain and stator domain are set to stationary. The rotor domain is set to rotate around the negative z-axis with a constant speed of 20 r/s. The alternate rotation model, in which the absolute frame velocity is advected instead of relative frame velocity, is chosen for a significant reduction in numerical error.

3.3. Verification of Grid

In order to assess the performance of PJP, the dimensionless hydrodynamic coefficients are defined as follows.

$$J = \frac{V_A}{nD_r},\ K_{Tr} = \frac{T_r}{\rho n^2 D_r^4},\ K_{Ts} = \frac{T_s}{\rho n^2 D_r^4},\ K_{Td} = \frac{T_d}{\rho n^2 D_r^4},\ K_T = \frac{T_r + T_s + T_d}{\rho n^2 D_r^4} = K_{Tr} + K_{Ts} + K_{Td}$$

$$K_{Qr} = \frac{Q_r}{\rho n^2 D_r^5},\ K_{Qs} = \frac{Q_s}{\rho n^2 D_r^5},\ \eta = \frac{TV_A}{2\pi n Q_r} = \frac{(T_r + T_s + T_d)V_A}{2\pi n Q_r} = \frac{J}{2\pi}\frac{K_T}{K_{Q_r}} \tag{6}$$

where J is the advance ratio. T is the thrust, with the subscript of r, s, d denote stator, rotor and duct. Q represents torque, Q_r and Q_s are the torque of rotor and stator, respectively. K_{Tr}, K_{Ts} and K_{Td} are the thrust coefficient of the rotor, stator, and duct, respectively. K_{Qr} and K_{Qs} are the torque coefficient of the rotor and stator, respectively. η is the open-water efficiency. During calculation, the rotor speed is fixed at 20 r/s. By adjusting the V_A, we can acquire the PJP's performance at various J.

This section mainly discusses the results of the K_T and K_{Qr} to verify the grid. The formulations will be illustrated by taking the K_T as example. The convergency ratio of thrust coefficient $R(K_T)$ is:

$$R(K_T) = \frac{S_2(K_T) - S_1(K_T)}{S_3(K_T) - S_2(K_T)} \tag{7}$$

where the 'S' with subscript '1', '2', '3' represent three different configurations with fine, medium, and coarse meshes. According to the results of $R(K_T)$, three conditions are obtained as follows:

(1) $0 < R(K_T) < 1$: Monotonic convergence.
(2) $-1 < R(K_T) < 0$: Oscillatory convergence.
(3) $|R(K_T)| > 1$: Divergence.

The uncertainty can be calculated by a correction of factor [33,34] or factor of safety [35]. The present work uses the factor of safety, i.e., value of 1.25 to calculate the uncertainty, which has an alternate definition: the Grid Convergency Index (GCI). The GCI for a fine mesh is defined as:

$$GCI_{Fine}^{21}(K_T) = \frac{1.25\delta_{21}^{a}(K_T)}{r^{p_l(K_T)} - 1} = U(K_T) \tag{8}$$

The following formulations are used to calculated the $GCI_{Fine}^{21}(K_T)$,

$$\begin{aligned} p(K_T) &= \frac{1}{\ln(r_i)}\left[\ln\left(\frac{S_3(K_T) - S_2(K_T)}{S_2(K_T) - S_1(K_T)}\right) + q(p(K_T))\right] \\ q(p(K_T)) &= \ln\left(\frac{r_{21}^{p_l(K_T)} - s(K_T)}{r_{32}^{p_l(K_T)} - s(K_T)}\right) \\ s(K_T) &= 1 * \mathrm{sign}\left(\frac{S_3(K_T) - S_2(K_T)}{S_2(K_T) - S_1(K_T)}\right) \\ \delta_{21}^{a} &= \left|\frac{S_2(K_T) - S_1(K_T)}{S_1(K_T)}\right| \end{aligned} \tag{9}$$

where the order of accuracy $p(K_T)$ is generally calculated by the fixed-point iteration method, but the refinement ratio r_i is set to a constant value of 1.4 in this work, which means the $q(p(K_T))$ is zero. Meanwhile, we can use the K_T and r_i to solve $p(K_T)$. Following the above steps, we can also obtain the CGI of K_{Qr}.

Table 3 lists the verification results under different J. The convergency ratio of K_T and K_{Qr} are all located between 0 to 1, illustrating that the mesh groups are monotonic convergence. Although the GCI of K_T and K_{Qr} are discrepant at different J, all of them are below 1%, demonstrating that the refinement of grid does not cause a significant change of hydrodynamic coefficients. In order to get a more detailed flow field, the fine mesh is adopted for a further study of the effect of the stator on the PJP's performance.

Figure 5 presents PJP performance curves with fine mesh. The curves of K_T, K_{Tr} and η are plotted in solid line. The dash lines are applied to other thrust coefficients and torque coefficients of PJP components. In addition, the experiment data of K_{Tr} and K_{Qr} [36] are given in the style of the symbol. The results show that the changing trend of K_T, K_{Qr}, and η is similar to conventional propellers. The difference is that η for PJP has a relatively large value in a wide range of J. The maximum η location is approximately 0.9 of J, where the η reach up to approximately 0.6. Furthermore, the duct generates additional effective thrust at low J, but produces resistance at high J; the turning point of J after which the duct never produce effective thrust is approximately 0.7. In contrast, the stator always provides drag force.

Table 3. Uncertainty analysis under different advance coefficients.

	J = 0.2		J = 0.4		J = 0.6	
	$\xi = K_T$	$\xi = 10K_{Qr}$	$\xi = K_T$	$\xi = 10K_{Qr}$	$\xi = K_T$	$\xi = 10K_{Qr}$
$S_1(\xi)$	0.6306	0.9818	0.6306	0.9818	0.6306	0.9818
$S_2(\xi)$	0.6284	0.9655	0.6284	0.9655	0.6284	0.9655
$S_3(\xi)$	0.6218	0.9403	0.5975	0.9152	0.6218	0.9403
$R(\xi)$	0.3447	0.6445	0.6579	0.8444	0.3493	0.7900
$p(\xi)$	3.1656	1.3054	1.2443	0.5025	3.1259	0.7005
$\delta_{21}^{a}(\xi)$	0.0036	0.0166	0.0058	0.0258	0.0013	0.0182
$GCI_{Fine}^{21}(\xi)$	0.0024	0.0376	0.0140	0.1751	0.0009	0.0857
	J = 0.8		J = 1.0		J = 1.2	
	$\xi = K_T$	$\xi = 10K_{QR}$	$\xi = K_T$	$\xi = 10K_{QR}$	$\xi = K_T$	$\xi = 10K_{QR}$
$S_1(\xi)$	0.5274	0.8669	0.4638	0.8062	0.3755	0.6867
$S_2(\xi)$	0.5263	0.8513	0.4632	0.7867	0.3751	0.6723
$S_3(\xi)$	0.5246	0.8288	0.4625	0.7622	0.3745	0.6512
$R(\xi)$	0.6683	0.6906	0.7390	0.8008	0.5705	0.6818
$p(\xi)$	1.1976	1.1003	0.8990	0.6603	1.6678	1.1386
$\delta_{21}^{a}(\xi)$	0.0021	0.0180	0.0012	0.0243	0.0010	0.0209
$GCI_{Fine}^{21}(\xi)$	0.0054	0.0501	0.0041	0.1220	0.0017	0.0561

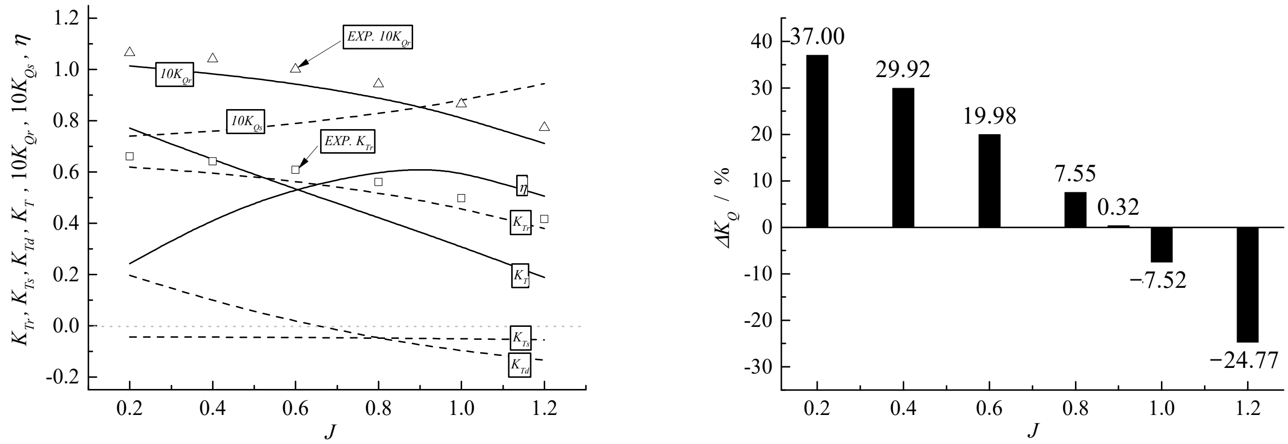

(**a**) Hydrodynamic coefficient curves (**b**) Torque difference between stator and rotor

Figure 5. PJP performance with fine mesh.

Comparing the K_{Tr} and K_{Qr} obtained by numerical simulation with the experimental data, it is evident that the numerical results at the whole range of *J* are relatively smaller than experiment data, especially at large *J*. The maximum error of K_{TR} and K_{QR} appears at *J* = 1.2 is 8%; other errors range 4%~7%. We think this relatively high error should be attributed to inherent numerical analysis, plus an unconformity with experimental environments, such as attachment used for fixing PJP components or relatively small flow tunnel may have an undesirable influence. However, the trend of numerical results corresponds well to experimental data. The numerical method is acceptable to get a further study on PJP. In addition, the torque directions of the stator and rotor are opposite to each other. The larger difference in rotor torque and stator torque may generate a high overturning moment for the submarine, affecting its maneuverability. Therefore, we define the torque difference ΔK_Q as $(K_{QR} - K_{QS})/K_{QS} \times 100$ for a quantitative evaluation. Figure 5b exhibits the ΔK_Q at different *J*. It is clear that the absolute value of ΔK_Q reduces first and then increase with the increase in *J*. The optimum condition is where the ΔK_Q equals zero, which means that the submarine does not need to produce extra force to balance the overturning moment. The balance condition of torque for the original PJP locates at slightly higher than 0.9 of *J*.

Figure 6 shows the contour of wall y^+ at J = 0.8. The rotor exhibits a high y^+ compared with the stator and duct. Meanwhile, the y^+ at the leading edges of the stator, rotor, and duct is relatively higher than at other regions. The mean y^+ at the stator and duct are 0.3 but 0.8 at the rotor, satisfying the turbulence model demand and is appropriate for high Reynolds number flow.

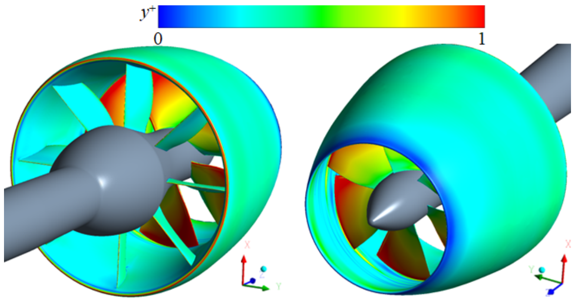

Figure 6. The y^+ distribution at wall under J = 0.8.

4. Flow Results of Different Stator Parameters

4.1. Influence of Stator Solidity

The stator solidity, determined by N_s and L, is generally one of the first key factors in the design procedure. The stator solidity increases proportionally to the increase in N_s or L. In order to compare the effect of these two parameters on the PJP's performance, the range and interval of stator solidity of N_s cases and L cases are kept the same.

A. Stator number

The hydrodynamic performance of PJP at J = 0.2~1.2 with five sets of stator numbers is presented in Figure 7, where the case of N_s = 8 represents the original case. As shown in Figure 7a, the thrust and torque of PJP increase linearly with the increase in N_s. The difference in total thrust and torque at low J between two adjacent N_s cases ranges 4% ~ 5%. The efficiency of PJP slightly changes or even presents a negligible change with the increase in N_s, and the maximum efficiency locates at J = 0.9. However, after the 0.9 of J, the efficiency reduces dramatically with the decrease in N_s, especially at J = 1.2. For instance, the efficiency of N_s = 6 at J = 1.2 is reduced by 16% relative to the original case. The thrust coefficients of PJP, which consist of K_{Tr}, K_{Ts}, K_{Td}, are plotted in histogram form in Figure 7b. It is clearly seen that the larger the N_s, the more resistance the stator creates. For each additional stator blade, the resistance increases by 2.5 N at J = 0.8, or causes an increase in K_{Ts} by 15%~20%. For K_{Tr} and K_{Td}, there is an approximate 5% and 2% increase, respectively. Figure 7c exhibits torque difference at the whole operating conditions. Generally, the change rules of torque and thrust with J are similar. That is, both K_{Qr} and K_{Qs} increase with the increase in N_s. However, the different increased rate of K_{Qr} and K_{Qs} with N_s eventually shifts the torque balance position. As N_s increase, the balance condition moves toward lower J. Specifically, the torque balance positions for N_s = 6~10 are located at 1.1, 1.0, 0.9, 0.8, and 0.7, respectively.

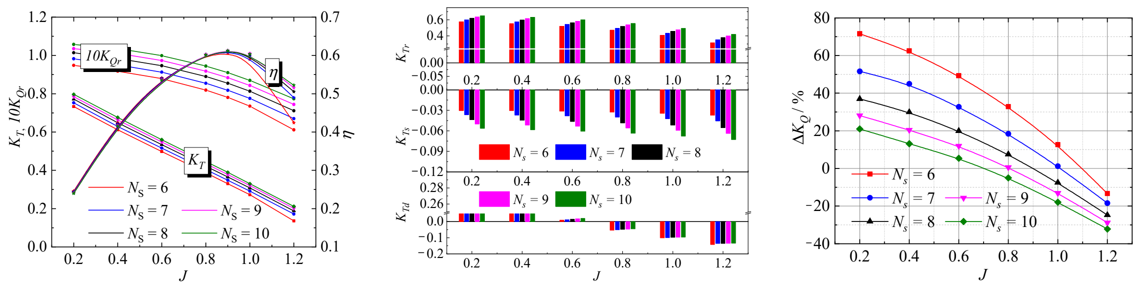

(**a**) Open-water performance (**b**) Thrust coefficient of different parts (**c**) Torque difference in stator and rotor

Figure 7. PJP performance with different stator number.

Figure 8 presents pressure contour at the plane of x = 0 and velocity contour at four different planes under J = 0.8 (principal analysis condition in later). The four planes are separately located upstream of the stator, in the middle of the stator, downstream of the stator, and upstream of the rotor. Note that the plane of A_4 located in the rotor domain, the variable 'velocity in stn frame', which denotes the absolute velocity, is plotted to avoid all-one-color at A_4 or other planes due to excessive velocity difference between stator domain and rotor domain. In addition, both the pressure and velocity are dimensionless quantities normalized by $0.5\rho V_A{}^2$ and V_A, respectively. The contour of C_P shows some local-low pressure regions which correspond to free vortices in the wake of the rotor. Results indicate that the local low-pressure position and magnitude are essentially unchanged as N_s varies. The velocity contours at A_3 and A_4 show some low-speed zones, and the shape of which get narrow from the hub to the shroud. The radial-going trail of the low-speed zone at A_3 resembles the form of the trailing edge of the stator.

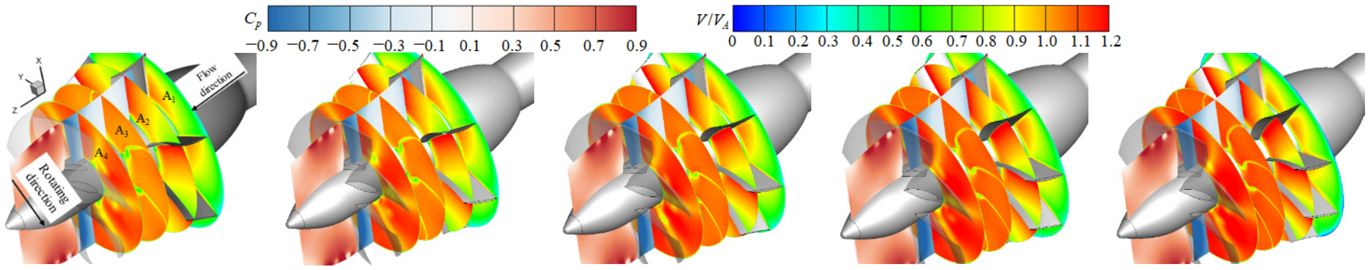

(**a**) $N_s = 6$ (**b**) $N_s = 7$ (**c**) $N_s = 8$ (**d**) $N_s = 9$ (**e**) $N_s = 10$

Figure 8. The contours of velocity and pressure.

Comparing the velocity contour at the surface of A_1~A_4, there is a significant acceleration effect for flow velocity. It is worth noting that flow velocity gradually becomes more uniform between two adjacent stator blades with N_s increase. Meanwhile, the velocity magnitude at A_3 is gradually increased from V_A to 1.2 V_A as N_s increases from 6 to 10. Since the larger N_s, the narrower flow passage between two adjacent stator blades and the more obvious acceleration effect it performs. The increased velocity of incidence flow for the rotor eventually causes an increase in rotor thrust. Since the increased amplitude of rotor thrust is greater than the resistance of stator, the total thrust of PJP keeps growing even though more drag is produced by added stator blade.

B. Chord length

It is necessary to investigate the effect of chord length on the PJP's performance before studying other paraments. Because when changing other paraments, such as stagger angle or sweep angle, the chord at each stator profile will vary inevitably. In this section, the chord is modified on the basis of N_s studied before. The chord of the original PJP is taken as a reference to other cases with extended foil or shrunken foil, namely L = 6/8C, 7/8C, 9/8C, and 10/8C. Figure 9 presents the performance of PJP with different chord length. In order to get a distinct contrast with the N_s effect, the ordinate scales are the same as that of Figure 7. According to the figures, the trend of all coefficients with L and with N_s is similar. The increase in K_T and K_{QR} range 3%~5% as L increase. The efficiency basically stays the same value at lower J but drops quickly at high J. Further, both K_{Ts} and K_{Tr} grow with the increase in L as rapidly as with the increase in N_s, and the K_{Td} also become larger as L increases when the duct produces thrust but become smaller when it generates drag. As for the torque difference, there are distinct differences of balance position between N_s configurations and L configurations under the same stator solidity. For L = 6/8C and 10/8C, the balance condition of J is slightly smaller than 1.1 and slightly higher than 0.7, respectively. However, for L = 7/8C and 9/8C, the balance conditions are the same as with the corresponding N_s cases (N_s = 7 and N_s = 9), i.e., J = 0.8 and J = 1.0, respectively.

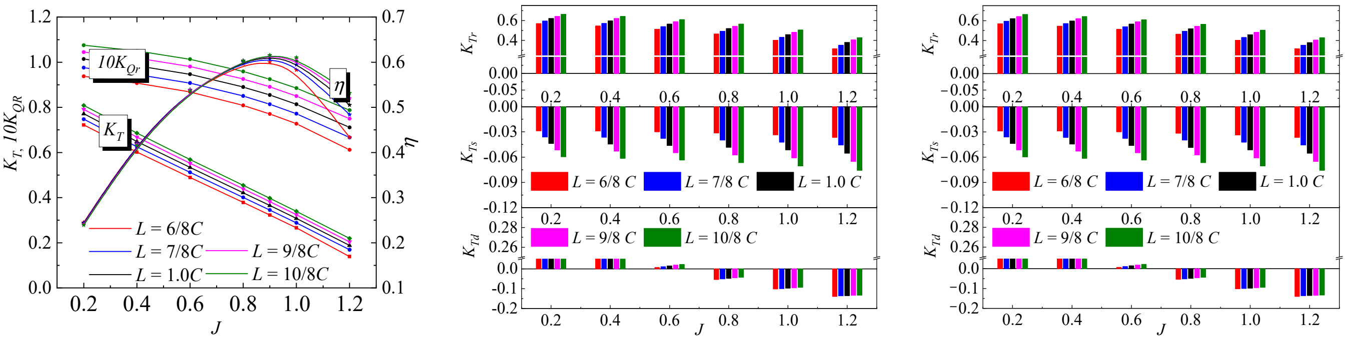

(**a**) Open-water performance (**b**) Thrust coefficient of different parts (**c**) Torque difference in stator and rotor

Figure 9. PJP performance with different chord length.

To further figure out the difference in the effect of N_s and L on the PJP's open-water performance, each hydro-coefficient difference between two sets under the same stator solidity is plotted in Figure 10. We define the difference as $\Delta\varphi = 100 \cdot (\varphi_1 - \varphi_2)/\varphi_2$, among which the φ represents hydrodynamic coefficients such as K_{Tr} or K_{Ts}, with the subscript '1' and '2' separately denote the coefficients of L and N_s configuration. The labels from 'conf.1' to 'conf.4' at the horizontal axis represent the cases of N_s = 6, 7, 9, 10, and each of them corresponds to L = 6/8C, 7/8C, 9/8C, 10/8C. Note that the conf.2 and conf.3 are reduced and increased stator solidity, respectively, based on the original PJP cases with a same magnitude, so are the conf.1 and conf.4.

As is shown in the figure, the difference in all coefficients under conf.1 is distinctly larger than conf.2. Take the K_{Tr} as an example, the $\Delta\varphi$ for K_{Tr} is 3.16% under conf.1, but reduces to 1.03% under conf.2; similarly, the $\Delta\varphi$ under the conf.4 is larger than that under the conf.3 except for the K_{Qs}, which illustrates the higher extent of stator solidity modified, the more distinct difference between N_s effect and L effect on the PJP's performance even under the same stator solidity. Furthermore, all the signs of coefficients for increased stator solidity are opposite to those for reduced except for K_{Qs}. For the increased stator solidity cases, i.e., the conf.3 and conf.4, the $\Delta\varphi$ are positive except for K_{Td}, which indicates the effect of L is more significant than N_s for increasing the PJP's thrust or efficiency, and the higher of stator solidity, the more obvious this effect. However, for the reduced stator solidity cases, i.e., the conf.1 and conf.2, the $\Delta\varphi$ is negative except for K_{Td} and K_{Qs}, which indicates the reduction in the N_s is more likely to deteriorate the PJP's performance compared with the decrease in L. Based on the above analyses, we can draw a conclusion that it is more obvious to modify L for the improvement of PJP's performance rather than adjust N_s.

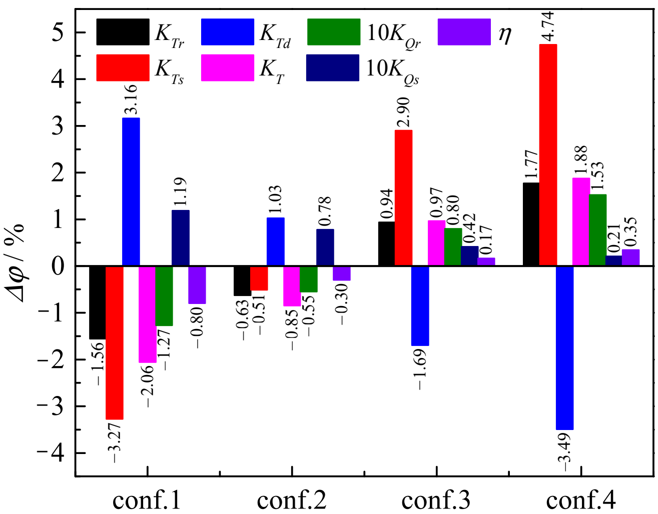

Figure 10. Hydro-coefficients difference under same stator solidity.

To further investigate the reason for the L effect on the PJP's performance, it is essential to study the flow field at and downstream of the stator. Figure 11 presents the C_P contour at the suction side and pressure side of the stator blade. The limiting streamlines are also exhibited. The label 'H' at ordinate represents the maximum span length in x-axis.

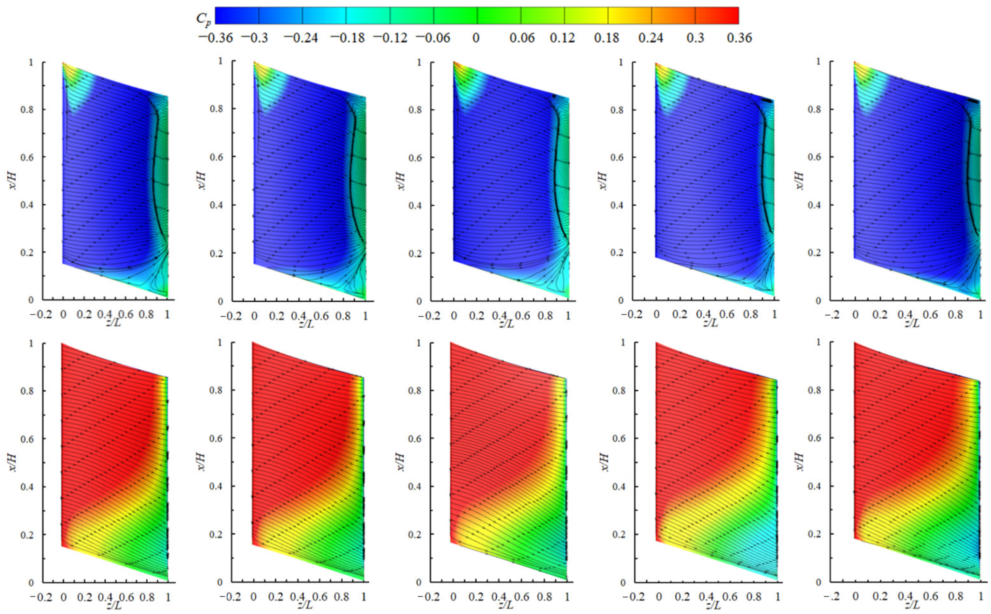

Figure 11. Limiting streamlines at stator (top: suction side; bottom: pressure side; the columns from left to right: L = 6/8C, 7/8C, 1.0C, 9/8C, 10/8C).

The contour of the pressure side presents a decrease in pressure from top left to bottom right, with streamlines parallel to the conic surface of the hub and shroud. It seems that the chord length L has little impact on streamline direction. The corner between the trailing edge and hub exhibits a low-pressure region that gradually enlarged with the increase in L. The results of the suction side surface show a local high-pressure region (axial direction: 0~0.3L, radial direction: 0.8~1H) in the corner between the shroud and leading-edge, which may be influenced by high stagnation pressure of duct inlet. The separation of the boundary layer occurs near the trailing edge. As L increases, the separation position moves downstream, namely from 0.8L to 0.9L. At the same time, the streamlines on the root of the suction side present radial-going flow and concentrate near the trailing edge. Furthermore, a small vortex is obviously presented close to the shroud and trailing edge. Due to the enormous pressure difference between the pressure side and suction side, together with a low-energy at the stator boundary layer, a secondary crossflow occurs, and the flow direction points to the hub.

Figure 12 presents the velocity distribution at the slice of A_3 and A_4. The figure shows narrow low-velocity regions along circumferential direction periodically. The periodicity of the low-speed zones at A_3 along circumference direction is consistent with N_s, i.e., eight; this is because of the occurrence of separation at stator trailing edge and its prolonged effect on downstream. However, the influence on location at A_4 by stator wake is not as strong as at A_3. Thus, the periodicity turns into six (the number of rotor blades), with some small strip-shaped and round-shaped low-speed regions existing due to the slight impact of stator wake. The results also show that a slight grow of velocity magnitude with the increase in L.

In order to investigate the flow details at A_3 and A_4, the velocity V and velocity components: axial velocity V_z, circumferential velocity V_c, radial velocity V_r along the circumferential direction at three different spans are presented in Figure 13. The circumferential angle at the horizontal axis is described in Figure 12. For the V_r, the direction from hub to shroud denotes positive; the opposite direction is negative.

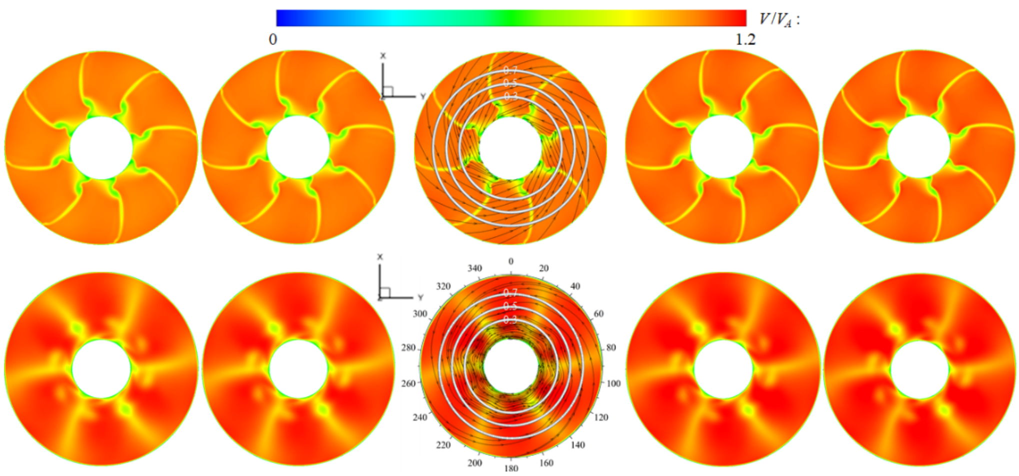

Figure 12. Velocity contour at the A_3 plane and the A_4 plane (top: A_3; bottom: A_4; the columns from left to right: L = 6/8C, 7/8C, 1.0C, 9/8C, 10/8C).

The velocity components change periodically except at 0.3span of A_4. The periodicity at A_3 is eight but six at A_4 except for V_r. However, the V_r at A_4 has the same periodicity as at A_3, which indicates V_r is deeply influenced by the stator. The stator effect is also observed at 0.3span of A_4, since there are induced peaks by stator blade for V_z and V_c, thus causing an uncertain periodicity. The proportions of the three velocity components vary greatly. Take the 0.3span of A_3 as an example, the V_z curves are especially close to V curves, meaning that the highest velocity proportion is V_z, the maximum value is above $0.9V_A$. Followed by the V_c, the maximum value is approximately 0.4 V_A.

Comparing the velocity components with various L, the large L seems to accelerate flow. Both V_z and V_c get larger as L increases. That explains why the larger L, the closer the boundary layer separation position to the trailing edge of the stator. In contrast, the L has little effect on V_r. The V_r curves at A_3 and A_4 under for various L cases almost coincide with each other. The resultant velocity finally has a 1.5%~2% increase with the increase in chord length.

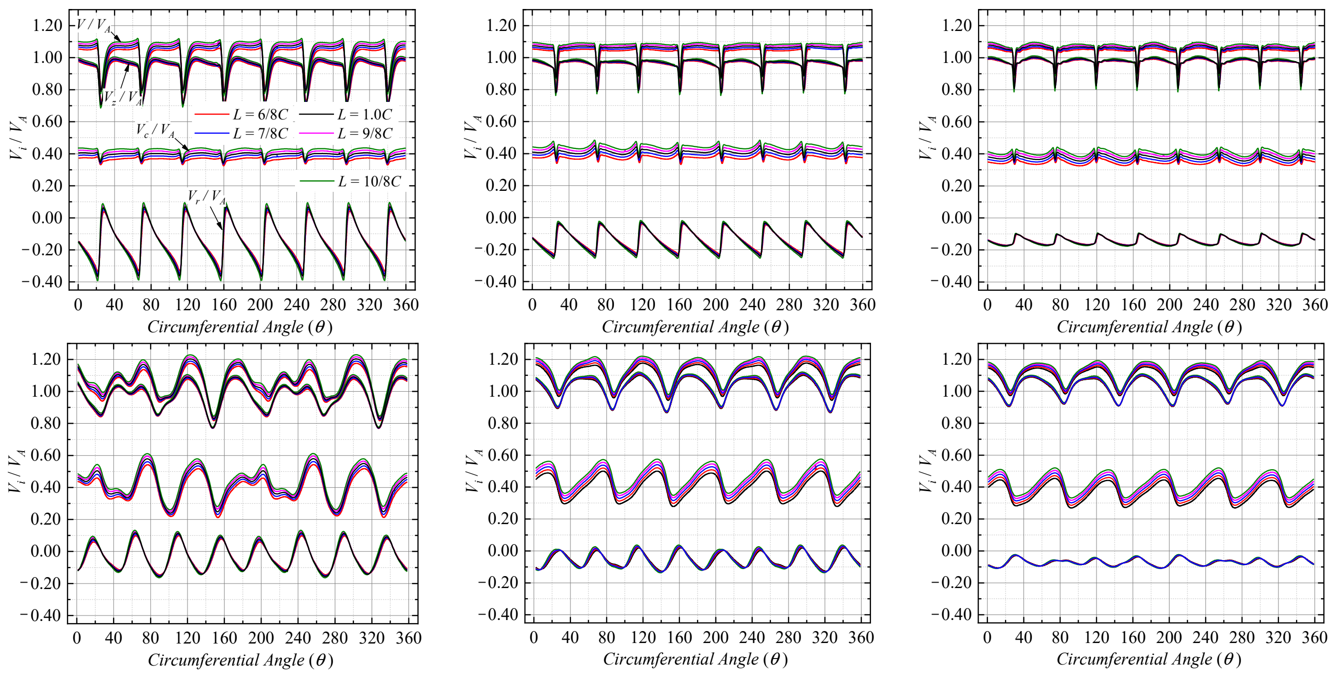

Figure 13. Detailed Velocity component (the rows from top to bottom: A_3, A_4; the columns from left to right: span = 0.3, 0.5, 0.7).

4.2. Influence of Stator Angles

The stator angles can be summarized as three parameters in cylindrical coordinate views as described previously: the stagger angle for the circumferential view, the lean angle for the axial view, and the sweep angle for the meridional view. Each parameter is modified with a same step (4°) to investigate and compare their effect.

A. Stagger angle

The stator stagger angle α is an essential parameter for PJP performance, since it greatly influences the effective incidence angle of rotor, while the blade height will be changed when adjusting the angle directly. Therefore, the chord length of hydrofoil at each section needs to be scaled to maintain a constant blade height. Table 4 lists the specific scaled factor of various angle cases of each stator profile.

Table 4. The scaled factor of various stator blade.

Cases	#1	#2	#3	#4	#5	#6	#7	#8	#9	#10
$\alpha = -4°$	0.9922	0.9903	0.9866	0.9833	0.9814	0.9804	0.9801	0.9808	0.9825	0.985
$\alpha = -8°$	0.9894	0.9856	0.9782	0.9719	0.968	0.9661	0.9655	0.967	0.9702	0.9751
$\alpha = 4°$	1.0128	1.0149	1.0188	1.0223	1.0245	1.0255	1.0259	1.025	1.0232	1.0205
$\alpha = 8°$	1.0311	1.0353	1.0436	1.0508	1.0554	1.0577	1.0584	1.0566	1.0528	1.0471

Figure 14 shows the PJP's performance with different α. In Figure 14a, as α increases, the K_T and K_{Qr} increase considerably. The α has a greatly obvious effect on the PJP's performance compared with the previous parameters. The growth rate of K_T from −8° to −4° is 13.96% relative to the former. The K_T increases by 13.78% from −8° to 0°, followed by 12.68% and 12.96% for 0° to 4° and 4° to 8°, respectively. The growth rates of K_{Qr} are 11.58%, 12.16%, 12.09%, and 13.7%, respectively, for −8° to −4°, ... , and 4° to 8°. The different growth rates of K_T and K_{Qr} eventually lead to a slight efficiency difference at $J = 0.8$, which is a turning point of the efficiency difference between various α cases. For $J < 0.8$, the η stays almost the same, but when J is greater or equal than 0.8, the η increase considerably as α increase. Further, the large α will cause the highest efficiency to move slightly toward high J.

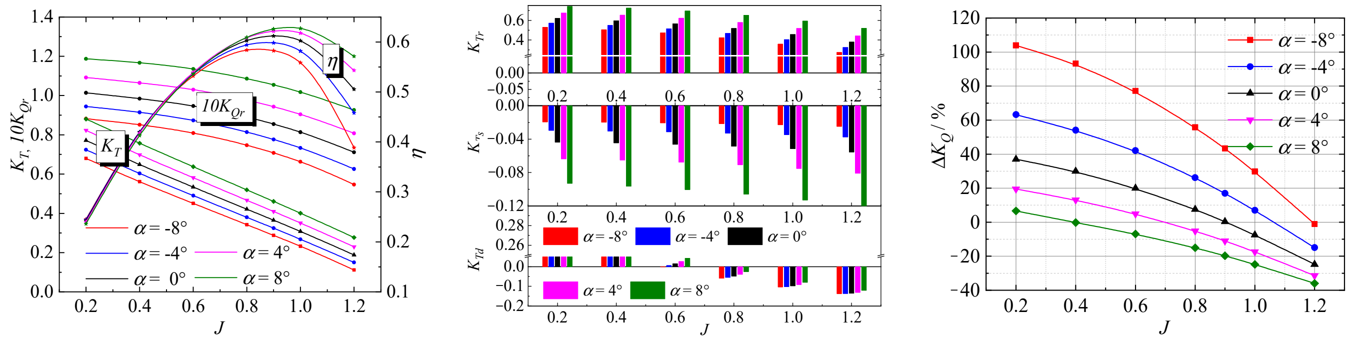

(**a**) Open-water performance (**b**) Thrust coefficient of different parts (**c**) Torque difference in stator and rotor

Figure 14. PJP performance with different chord length.

As shown in Figure 14b, the K_{Tr} and K_{Ts} positively correlate with α. However, for the K_{Td}, it increases with the increase in α when the duct provides thrust but decreases when the duct generates drag. In general, K_{Ts} and K_{Tr} are the most affected coefficients with the rise of α. The average growth rates for KTs and K_{Tr} are approximately 50% and 13% at $J = 0.8$.

Figure 14c exhibits a relatively larger torque difference value compared with the configurations of the previous two parameters. The maximum ΔKQ locates at $J = 0.2$

exceeds 100% when $\alpha = -8^\circ$. As α increases, the torque balance position moves toward low J. For $\alpha = -8^\circ \sim 4^\circ$. The balance points locate separately at J = 1.2, 1.05, 0.9, 0.7, 0.4.

Figure 15 shows the C_p contour for various cases at three different spanwise surfaces. Each subfigure exhibits only half of the computational domain for saving space. Obviously, the α has a dramatic influence on the pressure distribution in both stator and rotor domains. The pressure at the suction side of the stator and rotor reduces with the increase in α, but there is little change at the pressure side. It can be inferred that the rise of α will produce a larger stagnation pressure at the leading edge of the stator and cause the separation on the suction side of the stator to occur in advance. Meanwhile, the velocity flow direction is changed along the stator section as α increases and eventually leads to a larger attack angle for hydrofoil at each rotor blade section, which is similar to the function of increasing the pitch angle of the rotor. The large pressure-reduced area near the suction side of the rotor not only produces thrust and torque but may affect the contiguous region around the stator. The drag force caused by the stator is much higher at the same time when α increases, but the increased resistance of the stator is insufficient to offset the increased thrust of the rotor. Further, the increased rate of stator torque is also far less than the rotor. Consequently, the large α contributes to the increase in PJP total thrust and causes a higher torque difference at usual working conditions, further making torque balance point move to higher J. In addition, a strong change of pressure at 0.95 span near the tip of the rotor blade is observed, which results in tip leakage flow and rotor wake.

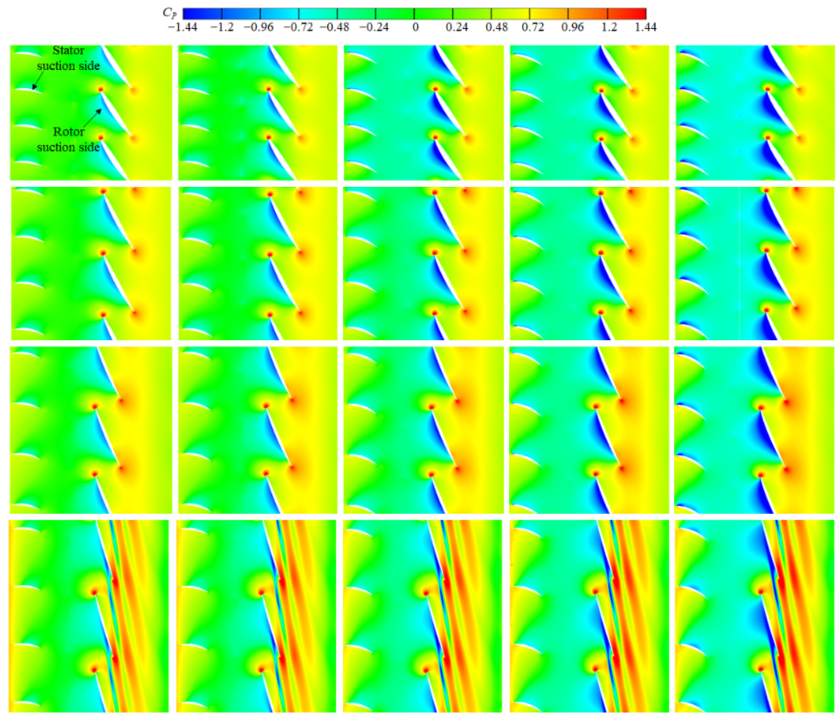

Figure 15. Pressure around stator and rotor blade sections under condition of J = 1 (the rows from top to bottom: span = 0.3, 0.5, 0.7, 0.95; the column from left to right: $\alpha = -8^\circ, -4^\circ, 0^\circ, 4^\circ, 8^\circ$).

B. Lean angle

In this section, the lean angle γ, as one of the secondary parameters in PJP design, is modified with the same step of 4° as α does. A series of PJP performances with various γ are presented in Figure 16. Similar to other previous parameters, as γ increases, K_T, K_{Qr}, and η all increase in varying degrees. The increased rate of K_T and K_{Qr} between two adjacent γ cases distributes in the range of 2%~4% at J = 0.8. In contrast, the η has a slight change but no more than 1%. For the component thrust, the K_{Tr} and K_{Ts} also increase linearly at 3% and 11% with the increase in γ, respectively. However, for K_{Td}, the relative variation between two adjacent configurations does not exceed 3%. As for torque difference, the change in ΔK_Q with γ is opposite to K_T or K_{Qr}. The maximum variation of ΔK_Q is located at J = 0.2 for $\gamma = -8°$, and it is smaller than that for previous parameters that have been analyzed. Consequently, the torque balance condition of J for $\gamma = -8°$ turns small, i.e., J = 1.0; For $\gamma = 8°$, it locates at J = 0.8. However, in other cases, the balance positions distribute between J = 0.8 and 1.0.

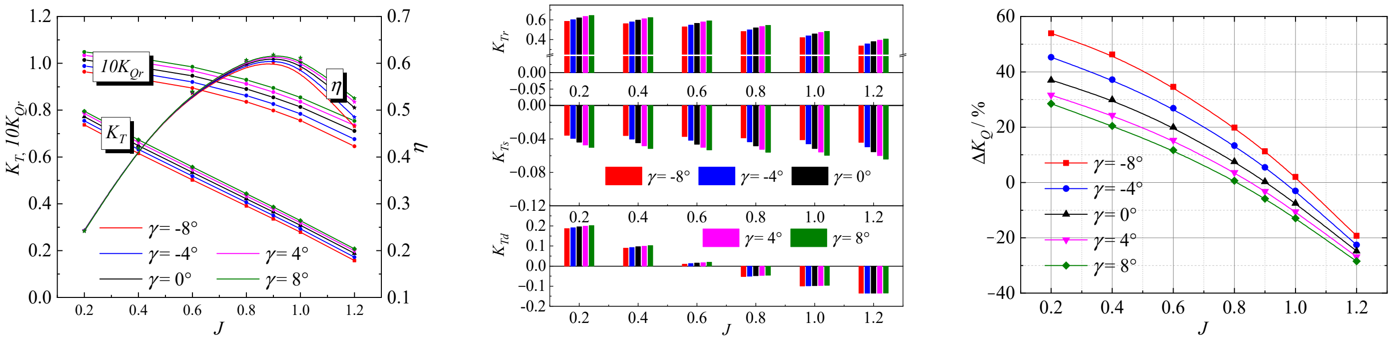

(**a**) Open-water performance (**b**) Thrust coefficient of different parts (**c**) Torque difference

Figure 16. PJP performance with different lean angle.

Further analysis on velocity distribution, as shown in Figure 17 between stator and rotor, is needed to better understand the reason for performance variation. As has been shown in Figure 12, there are six radial-going low-velocity-belts distributed evenly at constant Z plane due to stator wakes, with high-velocity between two adjacent belts. When γ increases, the velocity at the high-velocity region becomes slightly larger. The same phenomenon is obviously seen at 0.5 span, especially at the stator wake region. In Figure 18, the flow angle φ, defined as *arctan* (V_z/V_c), is presented at 0.5 span. It is found that φ decreases slightly with the increase in γ, especially at the region between stator and rotor. However, the decreased rate of flow angle is far less than the increased rate of velocity, thus causing an increase in K_T and K_{Qr}.

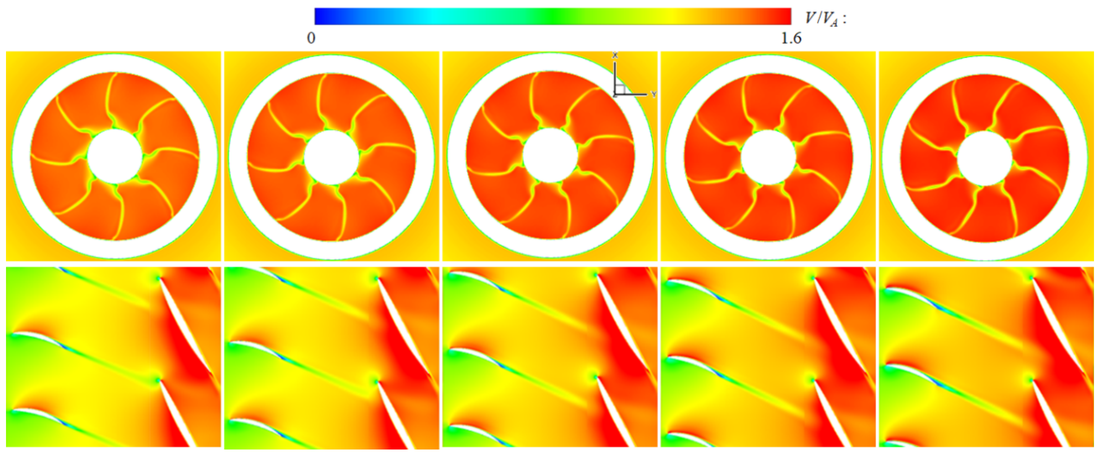

Figure 17. Velocity distribution at surface of A_4 and 0.5 span (top: A_3, bottom: 0.5 span; from left to right: $\gamma = -8°$~$8°$).

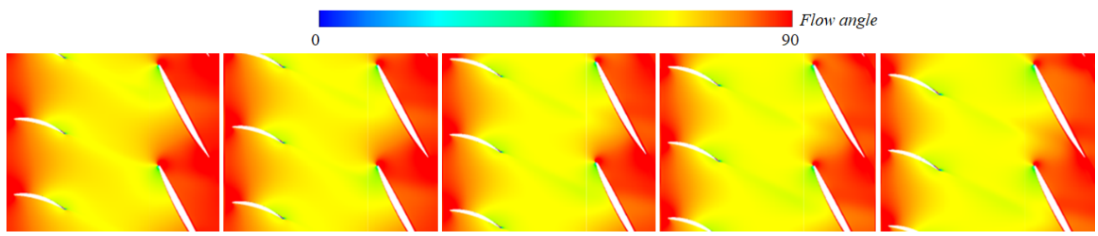

Figure 18. Flow angle at 0.5 span.

C. Sweep angle

In previous parameters, the stator always maintains a constant value of blade height to avoid the possible influence on the PJP's performance. In this section, we will investigate the global performance of PJP with various sweep angle β. Considering the mate dimensions of duct and stator, the lower bound of β is $-4°$, with a step length and upper bound are 4° and 12°, respectively. The open-water performance and thrust coefficient of all components are plotted in Figure 19a. The results show that the β has little effect on the performance of the rotor, with no more than a 1% difference in K_T, K_{Qr}, η between two different β situations without considering the off-design condition. The thrust of all components, including the stator, rotor, and duct, are plotted in Figure 19b. The K_{Tr} changes little. However, there are slight changes in K_{Ts} and K_{Td}. Take J = 0.8 as an instance, the K_{Ts} and K_{Td} separately decrease and increase with an average rate of 2% as a 4° step increase in β. Since both of K_{Ts} and K_{Td} are in the same order of magnitude, the resistance decreased on stator just offset the increased drag of duct, hence the thrust coefficient of PJP is essentially unchanged. For torque difference, a slight difference yields at low and high J compared with the original PJP, whereas the ΔK_Q stays almost the same at middle J, which results in a fixed torque balance position.

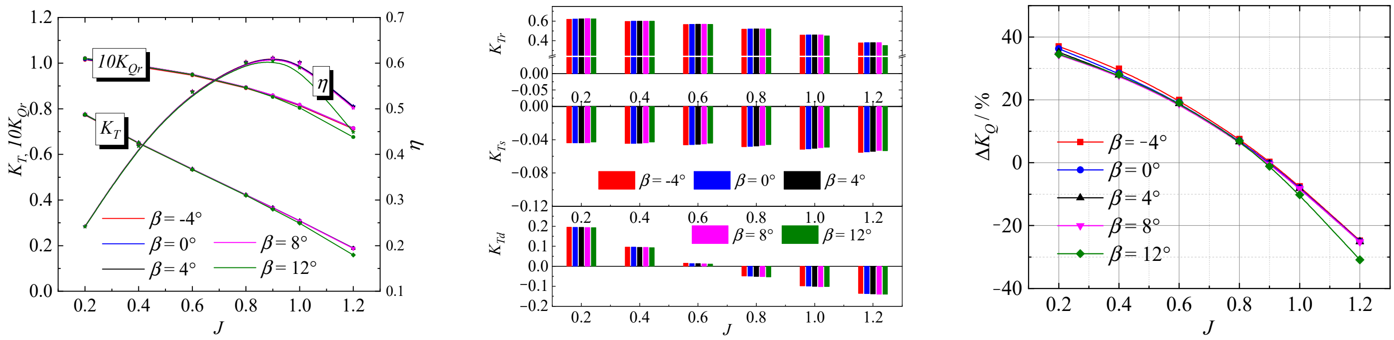

(**a**) Open-water performance (**b**) Thrust coefficient of different parts (**c**) Torque difference

Figure 19. PJP performance with different sweep angle.

Figure 20 presents the C_P at a constant span of 0.5. There are intense pressure changes at the leading edge and trailing edge. However, the curves of various β situations coincide with each other well. The same phenomena exist at other profile foils, thus demonstrating that changing β has essentially no effect on the pressure of the rotor.

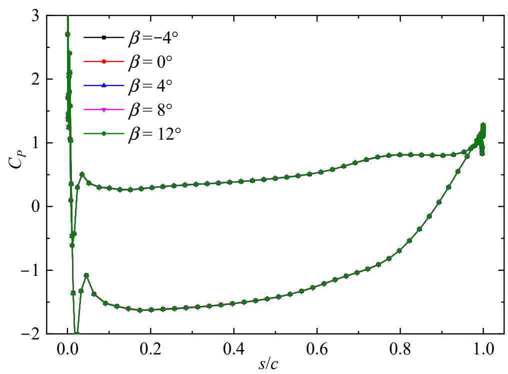

Figure 20. The static pressure coefficient of rotor at 0.5 span (s: the distance from leading edge; c: chord length).

The pressure coefficient of the stator blade is presented in Figure 21. The local high pressure in the upstream shroud-corner region on the suction surface for $\beta = -4°$ is much higher than for other cases. With the increase in β, namely the increase in the distance from the duct inlet to the high-span leading edge of the stator, the local high pressure gradually fades away. Finally, it forms a low-pressure belt at three sides, enclosing a much lower pressure region, which is obvious for high β. Thus, we can deduce that the pressure at the upstream shroud corner is deeply affected by the distance from the duct inlet to the leading edge of the stator. Compared with the negative β or lower β case, the higher β may benefit to structural performance due to a more uniform pressure distribution on the surface rather than a high local pressure that may result in stress concentration. Another noticeable phenomenon is that the concentrated point of streamlines near the hub and the trailing edge shifts slightly toward upstream when β increases. The vortex at the shroud corner of downstream is observed when β equals 8° and 12°, which will give rise to a large shear action on fluid tightly close to this area. Similarly, the *CP* of pressure surface at the upstream shroud-corner position is higher in the β equals −4° case than others, with the increase in β, the high-pressure area gradually reduced, thus causing the decrease in stator resistance.

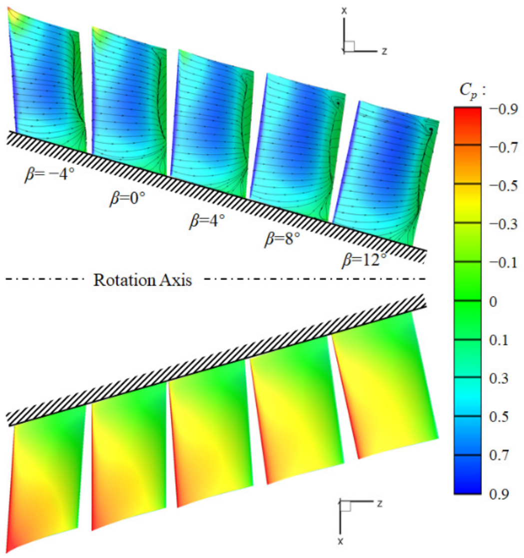

Figure 21. The C_P contour of stator blade (top: suction side covered with limiting streamlines; bottom: pressure side).

Figure 22 shows the velocity components *Vi* obtained from 0.5 span at the cut plane of A_3 and A_4. The influence of β on *Vi* at A_3 is more obvious than at A_4. A tiny distinction between various β cases is observed, while at A_4, the curves almost coincide. As for the flow angle, the maximum value is generally smaller at A_3 than at A_4. Specifically, the value of the flat part does not exceed 68° at A_3, but it is larger than 70° when the flow enters the rotor domain. Since the absolute increase in V_z is larger than V_c, the flow gradually deflects towards the axis direction after passing through the stator. It is also found that φ curves are much more identical at A_4 than at A_3 except for some special flat parts at A_4, thus explaining the identical pressure distribution of the rotor blade section for various β cases, as shown in Figure 20.

4.3. Influence of Rotor–Stator Spacing

The stator-rotor spacing *S* is an important parament in the design of PJP. Since the rotor–stator interaction become intense when the *S* becomes small and causes a disastrous hydro-oscillation force on the rotor. In contrast, a big *S* will cause hydraulic loss that may have an adverse impact on the performance of PJP. According to some design manuals, the values of *S* typically shall not be less than $0.05D_r$ in axial-flow pump design, and the smallest *S* modified in this paper far satisfy the devising standard. In this section, the interface stays the same location. Only the stator blades are moved toward the rotor. Numerical simulation settings remain the same except that the number of nodes in the stator domain is properly increased and decreased before and after the stator.

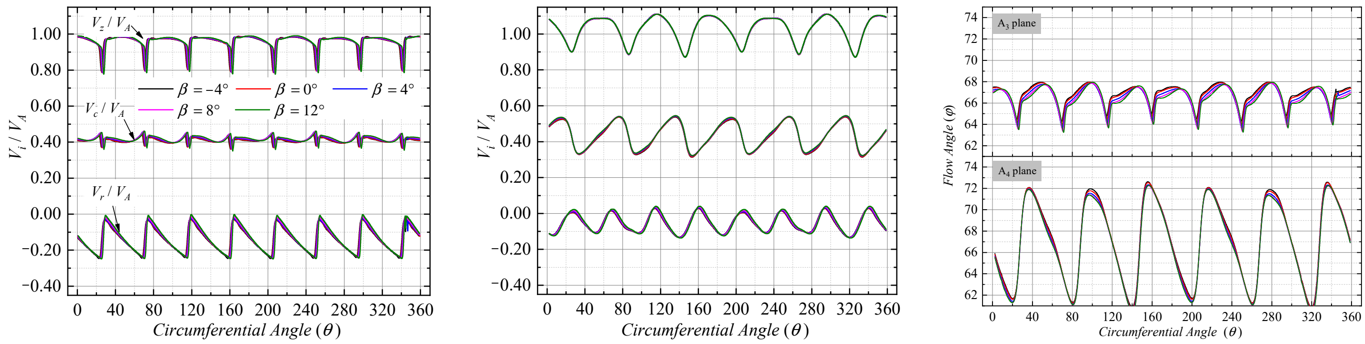

Figure 22. Velocity component and flow angle at 0.5 span (the first two columns: V_i at A_3 and A_4, respectively; the third column: flow angle at A_3 and A_4).

Figure 23 presents the performance of different S situations, the K_{Qr} and η of PJP are slightly affected by S, while the K_T gives the same value for all cases. By further studying the force of each component, it is found that the variation of force for duct and stator between all cases is highly varied than that of rotor force. For example, when J = 0.8, although the increased rates of K_{Ts} and K_{Td} are separately approximately 2.5% and 1.5%, the K_{Tr} increases less than 1%. Eventually, the K_T is almost unchanged because of one magnitude order larger than K_{Ts} and K_{Td} that K_{Tr} owns. For torque difference, as J reduces, the variation of ΔK_Q gradually becomes larger. The maximum difference between the case of maximum S and minimum S (i.e., 0.35Dr and 0.23Dr) is less than 10%. The balance conditions for all S cases regularly distribute at approximately J = 0.9.

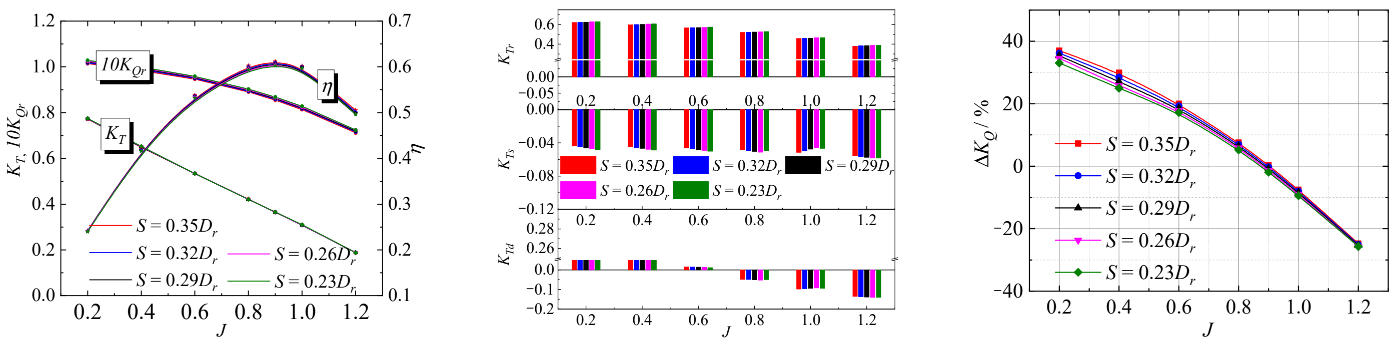

(**a**) Open-water performance (**b**) Thrust coefficient of different parts (**c**) Torque difference

Figure 23. PJP performance with different rotor–stator spacing.

Due to the slight change of K_{Tr}, the pressure curves at 0.5 span rather than pressure contour are presented in Figure 24 to investigate the main reason for slight change of the performance coefficients. The figure shows that the C_p at the pressure side has no change with variation of S. However, the C_p at the suction side decreases slightly with the reduction in S, especially within the range of 0~0.5 chord of the rotor. Thus, it causes a slight increase in KTR when S becomes smaller.

Figure 25 presents the velocity component at 0.5 span. Due to the frozen interface between stator and rotor, the flow is interrupted when entering into the rotor domain, thus causing the length of wake to decrease accordingly with the decrease in S, which is non-physical. The rotor acceleration is obviously seen in the figure of V_z contour. The V_z increases to approximately 1.4 V_A at the channel and wake of the rotor. However, the V_c, plotted in the absolute coordinate reference system, is close to zero on the pressure side, so are the regions after the rotor. However, the high V_c exists on the suction side of the rotor and stator. The difference is that the high V_c locates at the trailing edge of the stator, but it locates at the leading edge of the rotor. As for V_r, there are negative values in a wide area, especially near the pressure side of the stator, which demonstrates that the flow has a trend towards the hub. Additionally, the velocities distribution becomes more complicated as S decreases due to the more intense interaction between stator and rotor. Further transient simulation is worthwhile for the study of the fluctuant pressure and the PJP's oscillation force.

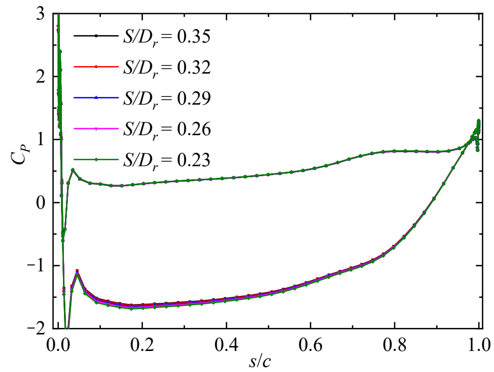

Figure 24. The static pressure coefficient of rotor at 0.5 span (s: the distance from leading edge; c: chord length).

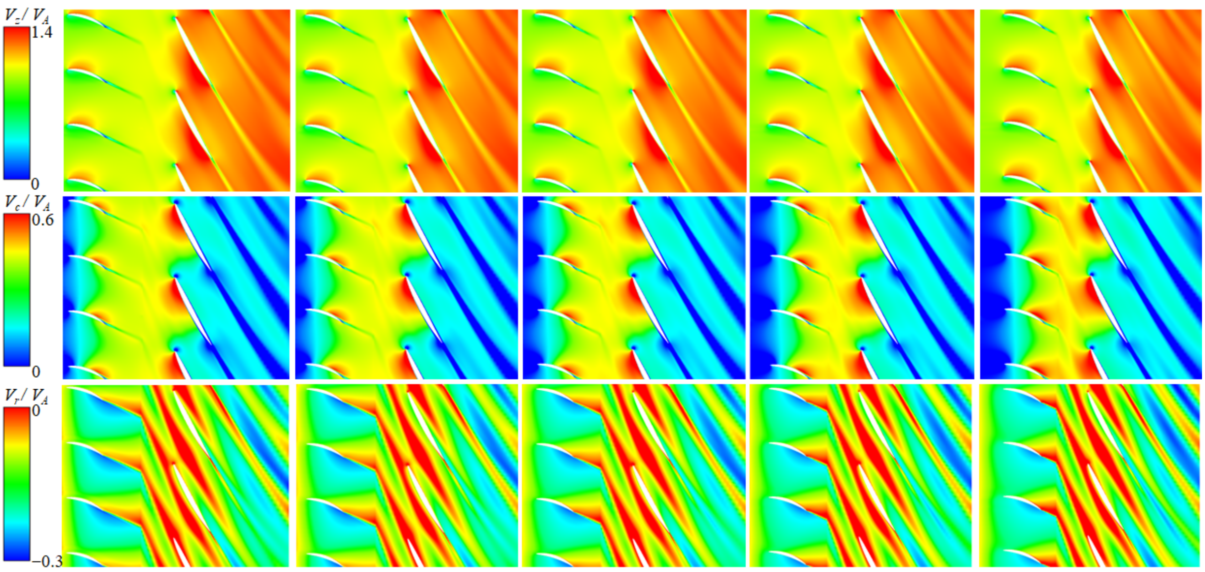

Figure 25. Contour of velocity component contour at 0.5 span (s: the distance from leading edge; c: chord length).

More specific velocity components along the circumferential direction of 0.5 span at A_3 and A_4 are plotted in Figure 26. It is evident that the lower S leads to a higher velocity at A_3. The maximum value of V_c increases tremendously with the decrease in S compared with V_z and V_r; however, the effect of S on the velocity at A_4 seems not as obvious as at A_3. The flow angle varies erratically at A_3, yet in most regions, it presents an increasing trend with the decrease in S; whereas at A_4, the change in flow angle becomes regular with S, i.e., increase slightly with S decreases, thus causing a slight increase in K_{Tr}.

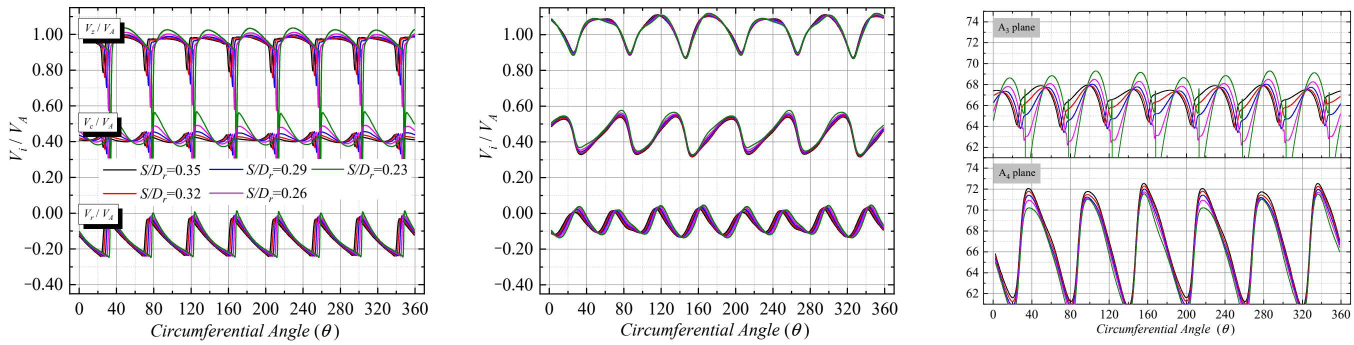

Figure 26. Velocity component and flow angle at 0.5 span (the first two columns: V_i at A_3 and A_4, respectively; the third column: flow angle at A_3 and A_4).

5. Conclusions

We have numerically investigated the hydro-performance of PJP with different stator parameters and classified these parameters into three groups:

(A) The blade number *Ns*, chord length *L*;
(B) The stagger angle α, lean angle γ, sweep angle β;
(C) The rotor–stator spacing *S*.

The SST *k*-ω turbulence model and frozen interface technique are employed to predict performance at various conditions. Based on RANS results, the verifications of mesh groups are performed to confirm appropriate mesh for further study. The results of the selected mesh give good accuracy with experiment results, which demonstrates the computation model is reasonable to predict the PJP's performance. To better understand why PJP global performance varies, we mainly analyze the global performance and flow results under $J = 0.8$, where the efficiency of the original PJP is a little lower than maximum efficiency. The numerical results are summarized as follows:

The parameters related to stator solidity, i.e., *Ns* and *L*, can accelerate flow when increasing them, yield higher incidence velocity for the rotor, and increase thrust and torque. At the same time, the efficiencies at design conditions stay almost the same. In addition, there are some distinctions between the two parameters for effect on PJP performance. The higher degree of stator solidity varies from the original PJP, the greater variation of results for two parameters.

The stator angles defined in various views are modified with the same step value (4°) to investigate their influence. The results indicate that *KT*, *KQr*, and η are positively associated with α and γ. However, no significant change occurs when adjusting β except for the off-design condition. The α has a greatly higher influence on the PJP's performance than the other two angles. The operating condition of *J* corresponding to maximum efficiency is shifted to a higher value when α increases. However, the γ only slightly affects the maximum efficiency, which increases with the increase in γ. In addition, we noted that a higher γ case gives a larger velocity and lower flow angle upstream of the rotor and eventually results in a rise of rotor thrust owing to a greatly higher change rate of velocity than flow angle. From the steady simulations, increasing α produces a large area of low-pressure regions on the suction side of the stator or rotor, which may lead to a higher fluctuation pressure and deteriorate the noise performance. In addition, the higher β, the lower chance of the local high-pressure region at shroud corner close to the leading edge of the stator, which can relieve the stress concentration without changing the PJP's performance and merits a further assessment.

The rotor–stator spacing has only a slight or limited influence on PJP performance. Even the stator has been translated towards the rotor 20 mm, or *S* decreases 34% relative to the original PJP, the rotor thrust at $J = 0.8$ rise only 1%, so does the K_{Qr} or η. Further investigation on the pressure coefficient of profile foil illustrates that *Cp* within 50% chord length from leading-edge becomes lower as *S* decrease.

Overall, among these stator parameters, the α mostly affects the PJP's global performance, followed by N_s and L, then is γ, the last two are S and β. In general, the torque and thrust for the blade (including stator and rotor) increase or decrease synchronously. The share of rotor thrust is extremely higher than the stator at design conditions. The increased K_{Ts}, caused by the increased α, stator solidity, or γ, does not significantly change K_T. In comparison, the duct provides thrust at heavy-loading conditions, which occupies 25% and 14% of the total thrust at J = 0.2 and J = 0.4 for the original PJP. A significant change of K_{Td} hence leads to an obvious change of K_T. For normal operating conditions, i.e., J = 0.8, the proportion of K_{Td} is as small as that of K_{Ts} and less than 10%, which is also not enough to change the total thrust. The ΔK_Q mainly is related to the change of K_{Qr}. The change rates of K_{Qr} for studied stator parameters are higher than K_{Qs}. The higher of K_{Qr}, the ΔK_Q becomes lower. Consequently, the J corresponding to torque balance location becomes lower.

Author Contributions: Conceptualization, F.L. and Q.H.; data curation, F.L.; investigation, F.L.; methodology, F.L.; visualization, F.L.; writing—original draft, F.L.; supervision, Q.H. and G.P.; writing—review and editing, Q.H., D.Q. and H.L. All authors have read and agreed to the published version of the manuscript.

Funding: This work is supported by the National Natural Science Foundation of China under Project Nos. 51979226 and by the Fundamental Research Funds for the Central Universities under Project Nos. 3102019HHZY030019 and 3102020HHZY030018.

Institutional Review Board Statement: Not applicable.

Informed Consent Statement: Not applicable.

Data Availability Statement: Not applicable.

Conflicts of Interest: The authors declare no conflict of interest.

References

1. Qin, D.; Huang, Q.; Shi, Y.; Pan, G.; Shi, Y.; Dong, X. Comparison of hydrodynamic performance and wake vortices of two typical types of pumpjet propulsor. *Ocean. Eng.* **2021**, *224*, 108700. [CrossRef]
2. McCormick, B.W.; Elsenhuth, J.J. Design and performance of propellers and pumpjets for underwater propulsion. *AIAA J.* **1963**, *1*, 2348–2354. [CrossRef]
3. Henderson, R.E.; McMahon, J.F.; Wislicenus, G.F. *A Method for the Design of Pumpjets*; ORL Report, No. 63-0209-0-7; Pennsylvania State Univ State College Ordnance Research Lab.: Centre County, PA, USA, 1964.
4. Furuya, O.; Chiang, W.L. *A New Pumpjet Design Theory*; Honeywell Inc.: Hopkins MN, USA, 1988.
5. Zierke, W.C.; Straka, W.A.; Taylor, P.D. An experimental investigation of the flow through an axial-flow pump. *J. Fluids Eng.* **1995**, *117*, 485–490. [CrossRef]
6. Suryanarayana, C.; Satyanarayana, B.; Ramji, K.; Saiju, A. Experimental evaluation of pumpjet propulsor for an axi-symmetric body in wind tunnel. *Int. J. Nav. Archit. Ocean. Eng.* **2010**, *2*, 24–33. [CrossRef]
7. Suryanarayana, C.; Satyanarayana, B.; Ramji, K. Performance evaluation of an underwater body and pumpjet by model testing in cavitation tunnel. *Int. J. Nav. Archit. Ocean. Eng.* **2010**, *2*, 57–67. [CrossRef]
8. Suryanarayana, C.; Satyanarayana, B.; Ramji, K.; Rao, M.N. Cavitation studies on axi-symmetric underwater body with pumpjet propulsor in cavitation tunnel. *Int. J. Nav. Archit. Ocean. Eng.* **2010**, *2*, 185–194. [CrossRef]
9. Shirazi, A.T.; Nazari, M.R.; Manshadi, M.D. Numerical and experimental investigation of the fluid flow on a full-scale pump jet thruster. *Ocean. Eng.* **2019**, *182*, 527–539. [CrossRef]
10. Lee, Y.T.; Hah, C.; Loellbach, J. Flow analyses in a single-stage propulsion pump. *J. Turbomach.* **1996**, *118*, 240–248. [CrossRef]
11. Ivanell, S. *Hydrodynamic Simulation of a Torpedo with Pumpjet Propulsion System*; Royal Institute of Technology: Stockholm, Sweden, 2001.
12. Das, H.N.; Jayakumar, P.; Saji, V.F.; Yerram, R. CFD examination of interaction of flow on high-speed submerged body with pumpjet propulsor. In Proceedings of the HIPER 06: 5th International Conference on High-performance Marine Vehicles, Launceston, Australia, 8–10 November 2006; Australian Maritime College: Newnham, Australia, 2006; p. 466.
13. Dong, Y.; Duan, X.; Feng, S.; Shao, Z. Numerical simulation of the overall flow field for underwater vehicle with pump jet thruster. *Procedia Eng.* **2012**, *31*, 769–774. [CrossRef]
14. Park, W.G.; Jang, J.H.; Chun, H.H.; Kim, M.C. Numerical flow and performance analysis of waterjet propulsion system. *Ocean. Eng.* **2005**, *32*, 1740–1761. [CrossRef]
15. Warn-Gyu, P.; Jung, Y.-R.; Kim, C.-K. Numerical flow analysis of single-stage ducted marine propulsor. *Ocean. Eng.* **2005**, *32*, 1260–1277.

16. Huyer, S.A. Postswirl maneuvering propulsor. *J. Fluids Eng.* **2015**, *137*, 9225. [CrossRef]
17. Ahn, S.J.; Kwon, O.J. Numerical investigation of a pump-jet with ring rotor using an unstructured mesh technique. *J. Mech. Sci. Technol.* **2015**, *29*, 2897–2904. [CrossRef]
18. Lu, L.; Pan, G.; Wei, J.; Pan, Y. Numerical simulation of tip clearance impact on a pumpjet propulsor. *Int. J. Nav. Archit. Ocean. Eng.* **2016**, *8*, 219–227. [CrossRef]
19. Lu, L.; Gao, Y.; Li, Q.; Du, L. Numerical investigations of tip clearance flow characteristics of a pumpjet propulsor. *Int. J. Nav. Archit. Ocean. Eng.* **2018**, *10*, 307–317. [CrossRef]
20. Qin, D.; Pan, G.; Huang, Q.; Zhang, Z.; Ke, J. Numerical investigation of different tip clearances effect on the hydrodynamic performance of pumpjet propulsor. *Int. J. Comput. Methods* **2018**, *15*, 1850037. [CrossRef]
21. Li, H.; Pan, G.; Huang, Q. Transient analysis of the fluid flow on a pumpjet propulsor. *Ocean. Eng.* **2019**, *191*, 106520. [CrossRef]
22. Yu, H.; Duan, N.; Hua, H.; Zhang, Z. Propulsion performance and unsteady forces of a pump-jet propulsor with different pre-swirl stator parameters. *Appl. Ocean. Res.* **2020**, *100*, 102184. [CrossRef]
23. Amini, Y.; Kianmehr, B.; Emdad, H. Dynamic stall simulation of a pitching hydrofoil near free surface by using the volume of fluid method. *Ocean. Eng.* **2019**, *192*, 106553. [CrossRef]
24. Menter, F. Zonal two equation kw turbulence models for aerodynamic flows. In Proceedings of the 23rd Fluid Dynamics, Plasmadynamics, and Lasers Conference, Orlando, FL, USA, 6–9 July 1993; p. 2906.
25. Rao, Z.Q.; Li, W.; Yang, C.J. Simulation of unsteady interaction forces on a ducted propeller with pre-swirl stators. In Proceedings of the Third International Symposium on Marine Propulsors, SMP, Launceston, Tasmania, Australia, 5–8 May 2013; Volume 13, pp. 149–155.
26. Lü, X.J.; Zhou, Q.D.; Bin, F.A.N.G. Hydrodynamic performance of distributed pump-jet propulsion system for underwater vehicle. *J. Hydrodyn.* **2014**, *26*, 523–530. [CrossRef]
27. Motallebi-Nejad, M.; Bakhtiari, M.; Ghassemi, H.; Fadavie, M. Numerical analysis of ducted propeller and pumpjet propulsion system using periodic computational domain. *J. Mar. Sci. Technol.* **2017**, *22*, 559–573. [CrossRef]
28. Qiu, J.T.; Yang, C.J.; Dong, X.Q.; Wang, Z.L.; Li, W.; Noblesse, F. Numerical simulation and uncertainty analysis of an axial-flow waterjet pump. *J. Mar. Sci. Eng.* **2018**, *6*, 71. [CrossRef]
29. Qiu, C.; Pan, G.; Huang, Q.; Shi, Y. Numerical analysis of unsteady hydrodynamic performance of pump-jet propulsor in oblique flow. *Int. J. Nav. Archit. Ocean. Eng.* **2020**, *12*, 102–115. [CrossRef]
30. Lu, L.; Wang, C.; Qin, D. Numerical investigations of flow characteristics of a pumpjet propulsor in oblique inflow. *Appl. Ocean. Res.* **2020**, *103*, 102343. [CrossRef]
31. Yuan, J.; Chen, Y.; Wang, L.; Fu, Y.; Zhou, Y.; Xu, J.; Lu, R. Dynamic analysis of cavitation tip vortex of pump-jet propeller based on DES. *Appl. Sci.* **2020**, *10*, 5998. [CrossRef]
32. Menter, F.R.; Kuntz, M.; Langtry, R. Ten years of industrial experience with the SST turbulence model. *Turbul. Heat Mass Transf.* **2003**, *4*, 625–632.
33. Wilson, R.; Stern, F. Verification and validation for RANS simulation of a naval surface combatant. In Proceedings of the 40th AIAA Aerospace Sciences Meeting & Exhibit, Reno, NV, USA, 14–17 January 2002; p. 904.
34. Wilson, R.; Shao, J.; Stern, F. Discussion: Criticisms of the "correction factor" verification method. *J. Fluids Eng.* **2004**, *126*, 704–706. [CrossRef]
35. Celik, I.B.; Ghia, U.; Roache, P.J.; Freitas, C.J. Procedure for estimation and reporting of uncertainty due to discretization in CFD applications. *J. Fluids Eng.-Trans. ASME* **2008**, *130*, 953. [CrossRef]
36. Li, H.; Huang, Q.; Pan, G.; Dong, X. The transient prediction of a pre-swirl stator pump-jet propulsor and a comparative study of hybrid RANS/LES simulations on the wake vortices. *Ocean. Eng.* **2020**, *203*, 107224. [CrossRef]